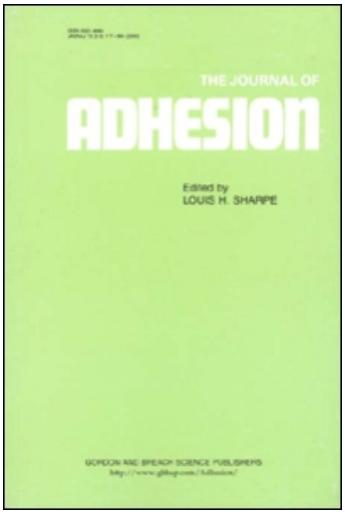

The Journal of Adhesion

Publication details, including instructions for authors and subscription information:
http://www.informaworld.com/smpp/title~content=t713453635

Viscoelastic and Nonlinear Adherend Effects in Bonded Composite Joints

Lezza A. Mignery[a]; R. A. Schapery[b]
[a] General Dynamics, Forth Worth, Texas, U.S.A. [b] Department of Aerospace Engineering and Engineering Mechanics, The University of Texas, Austin, Texas, U.S.A.

To cite this Article Mignery, Lezza A. and Schapery, R. A.(1991) 'Viscoelastic and Nonlinear Adherend Effects in Bonded Composite Joints', The Journal of Adhesion, 34: 1, 17 — 40
To link to this Article: DOI: 10.1080/00218469108026503
URL: http://dx.doi.org/10.1080/00218469108026503

J. Adhesion, 1991, Vol. 34, pp. 17–40
Reprints available directly from the publisher
Photocopying permitted by license only

Printed in the United Kingdom

Viscoelastic and Nonlinear Adherend Effects in Bonded Composite Joints

LEZZA A. MIGNERY

General Dynamics, Forth Worth, Texas 76039, U.S.A.

and

R. A. SCHAPERY

Department of Aerospace Engineering and Engineering Mechanics, The University of Texas, Austin, Texas 78712, U.S.A.

(Received March 19, 1990, in final form October 22, 1990)

An experimental and theoretical investigation is described on the effects of viscoelasticity and geometric and material nonlinearity in rubber-toughened graphite/epoxy adherends. Single-lap joints, with adherends of a matrix-dominated layup and a brittle epoxy adhesive layer, were tested under two constant loading rates to failure; axial strains were measured at several locations on the surface of the adherends. Aluminum and fiber-dominated laminate adherends were also studied for comparison. Finite element analyses of the adhesive joint were made using linear and nonlinear viscoelastic characterizations of the composite. The experimental work is discussed first. Then we describe the constitutive theory and its implementation in the finite element analysis, after which the theoretical ane experimental results are presented and compared.

KEY WORDS Adhesive joints; composite materials; viscoelasticity; nonlinear finite elements; fillets; single lap joints.

INTRODUCTION

The single-lap bonded joint assembly has been shown by many authors to have a highly complex state of stress in its adherends. Even though it is the most widely used joint for testing adhesives, the eccentricity in load path causes bending in the adherends which leads to geometrically nonlinear adherend behavior in the form of large transverse displacements.[1] In the case of composite adherends with a tough thermosetting or thermoplastic resin matrix, appreciable time dependence may be induced by the high stresses even in the absence of an extreme temperature environment. For the rubber-toughened, graphite/epoxy composite system studied, time-dependent matrix damage such as particle cavitation and microcracking (and possibly other changes in the microstructure such as shear banding) exists along with intrinsic viscoelasticity. Time-dependent nonlinear

material behavior (due to various sources) as well as large geometric nonlinearity (primarily due to adherend displacement) were accounted for in our mathematical model of the single-lap joint. Two different constant load rate tests, with a ratio of 100:1, were conducted on single-lap joint samples to determine the change in axial surface strain due to time-dependence and to observe any changes in failure behavior.

A particular angle-ply layup was selected for the adherend material that maximized nonlinear and viscoelastic effects and thus provided a critical test of the constitutive theory and structural analysis of the joint. A brittle epoxy was used for the adhesive layer in order to isolate primary time effects in the adherend material. For comparison, aluminum and 0° unidirectional adherend single-lap joints were also tested and analyzed.

Prediction of surface strains was made with a commercially available finite element program augmented with the constitutive equations for the graphite/epoxy; for comparison, a solution based on classical beam theory was also used, as described in the Appendix. The constitutive theory is based on a quasi-elastic version of the work-potential theory developed by Schapery,[2,3] which accounts for changes in the microstructure, such as damage, by a set of so-called structural parameters (or internal state variables). For instance, these parameters could be identified with statistical averages of the geometry of cracks and voids in the material. The specific constitutive equation presented here uses a structural parameter which is similar in form to the octahedral shear stress in the matrix of a composite lamina.[4] The analytical form of the lamina compliances is similar to that of Sun and Chen[5] without time-dependence; however, unlike their plasticity development, the model used here has been shown theoretically and experimentally to be descriptive of nonproportional as well as proportional loading.[2,6,7] This work-potential model was added to the finite element program ABAQUS (Hibbitt, Karlsson, and Sorenson, Version 4.5)[8] in order to predict surface strains.

Materials and experimental methods are described first. A brief description of the work-potential theory along with its implementation into the finite element program is then provided. Finally, experimental and theoretical results are compared. Space limitations preclude giving a detailed account of all experimental and theoretical work. For additional details the interested reader is referred to Mignery's dissertation,[6] upon which most of this paper is based.

MATERIALS AND EXPERIMENTAL METHODS

Hexcel T20 145 F155-76 graphite/epoxy was used for the composite adherend materials with two different layups, unidirectional $[0]_{8T}$ and angle-ply $[\pm 40]_{2S}$. The 0° laminate and aluminum (6061–T6) were chosen in part to check prediction capabilities without time dependence, and the angle-ply laminate was selected to maximize nonlinear and viscoelastic effects. The specimen configuration is shown in Figure 1. The composite specimens were cut from 12×12 in. plates of

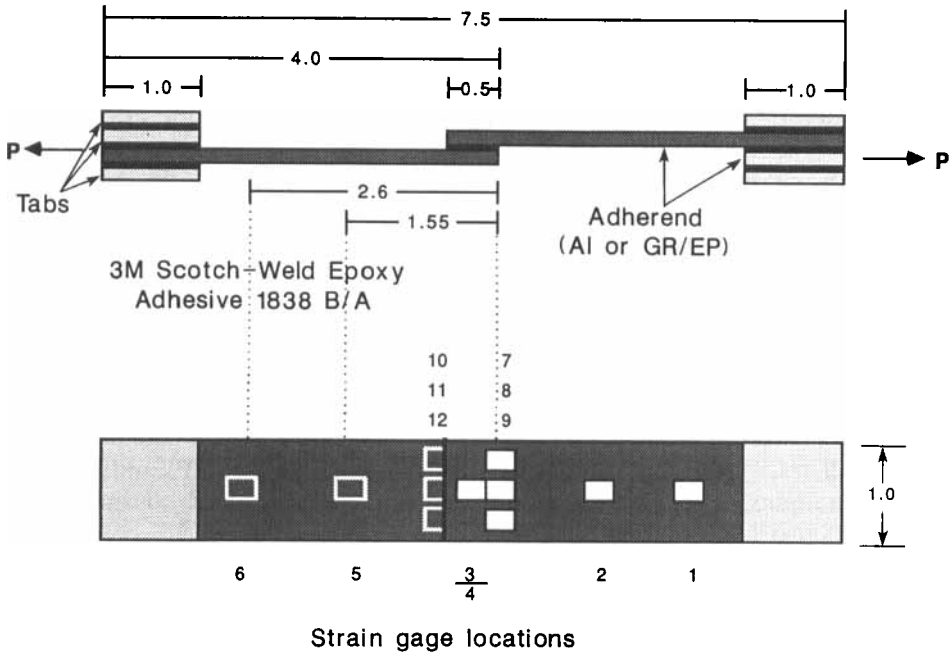

FIGURE 1 Lap joint specimen dimensions and strain gage locations. All dimensions are in inches. Gage locations are noted in the bottom figure by a rectangle. Those outlined in white appear on the opposite side of the joint.

graphite/epoxy material having a fiber volume fraction of 57 percent; they were made from prepreg tape and cured according to the manufacturer's specifications. Joint assemblies were formed by cutting 4.5 in. by 4.0 in. plates to be bonded together with a 0.5 in. overlap. The overlap area was sanded, wiped with acetone solvent and then measured for later bondline thickness determination. Just prior to bonding, the composite plates were further solvent wiped and the aluminum was vapor degreased. As shown in Figure 1, tabs were used to grip the legs and to ensure essentially axial alignment in the test machine. The alignment tabs were made of the adherend material. Additional tabs for gripping were bonded on both ends of each specimen. All adhesive bonds were made from 3M Scotch Weld 1838 B/A epoxy adhesive. This adhesive was used because of its essentially linear elastic behavior, thereby isolating most of the viscoelastic effects in the adherend material. The plates with tabs were assembled in a special jig to ensure uniformity of bondline thickness. They were heated to 150°F for 2 hours under 5 psi pressure for bond cure.

Specimens were then cut to 1.0 in. wide, corresponding to the dimensions given in the standard single-lap joint test, ASTM D1002-72. The only dimension not held to this standard was the thickness of the graphite/epoxy adherends. Nominal thicknesses for the aluminum and composite adherends were 0.06 in. and 0.05 in., respectively. The nominal adhesive thickness was 0.006 in. Specimens were

strain-gaged with Micro-Measurements CEA-06-062UW-350 gages to measure axial strains. The gage locations and the final specimen assembly are shown in Figure 1. Those gages remote to the overlap region were used to verify near-boundary conditions under loading, being placed close to the grip application points (gages 1 and 6), and to observe the strain in the straps or legs, being placed approximately at the center of the legs (gages 2 and 5). In the overlap region, gages 3 and 4 were placed opposite one another in the center of the overlap while gages 7–12 were placed directly opposite the edge of the overlap. These latter gages were used in part to check for variations across the width.

Aluminum and angle-ply samples were then tested at two different constant load rates to failure, 5 lb/s and 0.05 lb/s; the aluminum specimens showed, as expected, no significant effect of rate. The 0° samples were tested only at 5 lb/s. Testing was done in a fixed-grip MTS axial precision machine, with strain measurements taken during loading by an HP9845 computer and data acquisition system. All tests were conducted under room temperature (75°F) and humidity (50%) conditions. The material characterization tests involved constant stress rate, constant strain rate, and creep tests as described elsewhere.[6]

THE COMPOSITE MATERIAL CONSTITUTIVE THEORY

The Hexel F155 material is a rubber-toughened graphite/epoxy which is measurably viscoelastic at room temperature. With the angle-ply layup $[\pm 40]_{2S}$, this material has been observed to be strongly nonlinear above 30% of ultimate stress and to have a failure strain of nearly 7%; the creep strain at 40% of ultimate stress increases by 45% in 15 minutes.[6] As already noted, our material characterization is based on a work-potential theory and the quasi-elastic approximation. For a linear or nonlinear *elastic* material, the work potential W is simply the strain energy density. For an inelastic, *time-independent* material (with or without damage growth), W is the total work input for a unit initial volume, considering the entire history of loading. For monotone loading of a viscoelastic material with damage growth, one may often approximate the mechanical response using a work potential in which time enters as a parameter; this aging-like formulation is based on the quasi-elastic approximation of convolution integrals[9] and an approximate integration of the viscoelastic damage growth equations.[2] That a work potential exists for this material (at any given time) under proportional and nonproportional axial-torsional deformations has been shown by Lamborn and Schapery.[10]

In another application of the work potential theory to the characterization of laminates, only two-dimensional (in-plane) loading was taken into account.[7] In the present application, through-the-thickness normal and shear stresses exist in the lap joint region and thus a three-dimensional theory is needed. The constitutive equations given below are expressed in terms of principal material coordinates (x_1, x_2, x_3) for a unidirectional ply. Standard tensor transformation equations may then be used to refer them to the lap-joint coordinates (x, y, z).

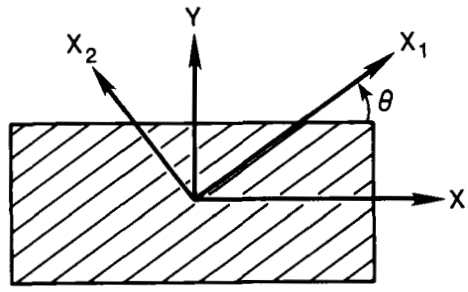

FIGURE 2 Unidirectional ply and coordinates.

Figure 2 shows a unidirectional laminate or ply and the coordinate notation, in which the x_1 axis is parallel to the fibers; the x_3 axis is normal to the ply plane. The stresses σ_i and strains ε_i $(i = 1, 2, \ldots, 6)$ are referred to the principal material coordinates x_i. In this discussion it will be convenient to use this single index notation. As is customary, $i = 4, 5, 6$ are used for the shearing variables; the relationship between single and double indexed tensor components is

$$\begin{aligned} &\sigma_{11} = \sigma_1, \quad \sigma_{22} = \sigma_2, \quad \sigma_{33} = \sigma_3, \quad \sigma_{23} = \sigma_4, \quad \sigma_{13} = \sigma_5, \quad \sigma_{12} = \sigma_6 \\ &\varepsilon_{11} = \varepsilon_1, \quad \varepsilon_{22} = \varepsilon_2, \quad \varepsilon_{33} = \varepsilon_3, \quad 2\varepsilon_{23} = \varepsilon_4, \quad 2\varepsilon_{13} = \varepsilon_5, \quad 2\varepsilon_{12} = \varepsilon_6 \end{aligned} \tag{1}$$

In terms of the single index strains, the work potential density (*i.e.* work/initial volume) for a ply is $W = W((\varepsilon_{ij}, t)$, where t arises from the effects of viscoelasticity, as discussed above. The stresses are given by

$$\sigma_i = \partial W / \partial \varepsilon_i \tag{2}$$

The work W and stresses in Eq. (2) are independent of strain history. However, this independence is approximately true for only limited, simple histories,[2] such as those considered in this paper.

We have found that a simple analytical description of the stress–strain equations is possible if stresses, rather than strains, are used as the independent variables. The inverse of Eq. (2) may be obtained in the usual way by means of a complementary work potential density $W_c = W_c(\sigma_i, t)$,

$$W_c \equiv -W + \sigma_i \varepsilon_i \tag{3}$$

(The summation convention is employed in that repeated indices imply summation over the index range.) By taking the total differential of Eq. (3) and then using Eq. (2) we obtain

$$\varepsilon_i = \partial W_c / \partial \sigma_i \tag{4}$$

In the linear viscoelastic range,

$$W_c \equiv \tfrac{1}{2} S_{ij}(t) \sigma_i \sigma_j \tag{5}$$

where the compliances $S_{ij}(t)$ of the composite under investigation have been found to have the form of a so-called generalized power law,

$$S_{ij}(t) = S_{ij}^0 + S_{ij}' t^q \tag{6}$$

where S^0_{ij} and S'_{ij} are constants; many vanish in view of the transverse isotropy of the ply and the negligible creep for loading in the fiber direction. The exponent q is a positive constant.

In the nonlinear range we found that

$$W_c = W_0 + W_1 t^q \tag{7}$$

where

$$W_0 \equiv \tfrac{1}{2} S^0_{ij} \sigma_i \sigma_j, \tag{8}$$

$$W_1 = A \tau_s^r \tag{9}$$

and $\tau_s = \tau_s(\sigma_i)$ is a quadratic function of the stresses; also, A and r are positive constants. The start of the nonlinear range is defined by a particular value of τ_s; when $\tau_s \leq \tau_c$, where τ_c is a positive constant, the linear form of W_c, Eq. (5), is to be used. Only loading behaviour is considered here; in order to account for differences between stress–strain behavior for unloading and loading it would be necessary to modify the form of W.[7]

Motivation for selection of a single quadratic function of stress τ_s to characterize the nonlinear behavior comes from the much earlier work of Lou and Schapery.[4] It was found that such a parameter accounted for the effect of stress state on the functions used to characterize nonlinear viscoelastic behavior of a glass/epoxy composite with various levels of constant damage; here, we do *not* assume the damage is constant. The form of this parameter was based on the observation that the octahedral shear stress τ_{oct} normally can be used to correlate multiaxial yielding of plastics (just as for metals). As a simplification, the matrix was viewed as a uniformly stressed layer of material sandwiched between layers of rigid fiber material; *i.e.*, the lines in Figure 2 at the angle θ were imagined to define layers rather than fibers. Using the principal material axes, this shear stress is

$$\tau_{oct} = \tfrac{1}{3}[(\bar{\sigma}_1 - \bar{\sigma}_2)^2 + (\bar{\sigma}_2 - \bar{\sigma}_3)^2 + (\bar{\sigma}_3 - \bar{\sigma}_1)^2 + 6(\bar{\sigma}_4^2 + \bar{\sigma}_5^2 + \bar{\sigma}_6^2)]^{1/2} \tag{10}$$

where the $\bar{\sigma}_i$ in this equation are the stresses in a matrix layer. For a uniformly stressed matrix $\bar{\sigma}_2$ and $\bar{\sigma}_6$ are the same as the stresses σ_2 and σ_6 acting on a composite consisting of parallel layers of matrix and reinforcement material. A constant factor ν_e was also introduced, as defined by the relationship $\bar{\sigma}_1 = \nu_e \sigma_2$. For a linear elastic, isotropic matrix in plane stress ν_e is the Poisson's ratio, and for an incompressible elastic or rigid-plastic matrix $\nu_e = 0.5$. Use of these idealizations in Eq. (10) yielded for plane stress ($\bar{\sigma}_3 = \bar{\sigma}_4 = \bar{\sigma}_5 = 0$),

$$\tau_{oct} = (2/3c)^{1/2}(\sigma_2^2 + c\sigma_6^2)^{1/2} \tag{11a}$$

where

$$c \equiv 3/(1 - \nu_e + \nu_e^2) \tag{11b}$$

As reported by Lou and Schapery,[4] a finite element analysis of a linear elastic composite with a square array of fibers was made to predict the average octahedral shear stress in the matrix. Apart from a numerical factor, Eq. (11) was found to be fairly good approximation to this average.

Returning to Eq. (10) for a three-dimensional stress state, we use the transverse isotropy of the actual composite to obtain

$$\bar{\sigma}_1 = \nu_e(\sigma_2 + \sigma_3) \tag{12}$$

Also, let

$$\sigma_4^2 = \eta'\bar{\sigma}_4^2, \qquad \sigma_5^2 = \eta'\bar{\sigma}_5^2, \qquad \sigma_6^2 = \eta''\bar{\sigma}_6^2 \tag{13}$$

where η' and η'' are free constants, just as c or ν_e. Additionally, for simplicity in notation, let

$$\tau_s \equiv 3c_1\tau_{\text{oct}}^2/2, \qquad c_1 = 1 - \frac{c}{2}, \qquad c_2 = \eta' c, \qquad c_3 = \eta'' c \tag{14}$$

Equation (10) now becomes

$$\tau_s = \sigma_2^2 + \sigma_3^2 + 2c_1\sigma_2\sigma_3 + c_2\sigma_4^2 + c_3(\sigma_5^2 + \sigma_6^2) \tag{15}$$

which is the function of stress $\tau_s = \tau_s(\sigma_i)$ appearing in Eq. (9).

The strains may now be derived from Eqs. (4)–(9) and (15). We may write the result in the form

$$\varepsilon_i = S_{ij}\sigma_j \tag{16}$$

The compliances S_{ij} are given by Eq. (6) for the linear range. To find S_{ij} for the nonlinear range, observe that

$$\varepsilon_i = S_{ij}^0\sigma_j + Ar\tau_s^{r-1}\frac{\partial\tau_s}{\partial\sigma_i}t^q \tag{17}$$

and $\partial\tau_s/\partial\sigma_1 = 0$. Thus,

$$S_{1j} = S_{j1} = S_{1j}^0 \tag{18a}$$

Also,

$$S_{22} = S_{33} = S_{22}^0 + 2Ar\tau_s^{r-1}t^q \tag{18b}$$

$$S_{23} = S_{32} = -\nu_{23}S_{22}^0 + 2c_1Ar\tau_s^{r-1}t^q \tag{18c}$$

$$S_{44} = 2(1+\nu_{23})S_{22}^0 + 2c_2Ar\tau_s^{r-1}t^q \tag{18d}$$

$$S_{55} = S_{66} = S_{66}^0 + 2c_3Ar\tau_s^{r-1}t^q \tag{18e}$$

where ν_{23} is the through-thickness Poisson's ratio in the linear range, $\nu_{23} = -S_{23}^0/S_{22}^0$. All other $S_{ij} = 0$. Note that transverse isotropy has been assumed for the composite. At the point of transition from linear to nonlinear behavior, $\tau_s = \tau_c$, the compliances in Eq. (6) must equal those in Eq. (18). This implies

$$S_{1j}' = 0 \tag{19a}$$

$$\tau_c^{r-1} = S_{22}'/2rA, \qquad c_1 = S_{23}'/S_{22}' \tag{19b}$$

$$c_2 = S_{44}'/S_{22}', \qquad c_3 = S_{66}'/S_{22}' \tag{19c}$$

Thus, in principle, after the linear viscoelastic compliances have been found one may derive c_1, c_2, and c_3. Nonlinear data for any *one* of the compliances may then be used to derive A and r; in turn, Eq. (19b) yields τ_c.

TABLE I
Material constants of the graphite/epoxy composite used in the finite element analysis

Material constant	Value
S_{11}	0.062×10^{-6} (psi)$^{-1}$
S_{12}	-0.022×10^{-6} (psi)$^{-1}$
S_{22}^0	0.696×10^{-6} (psi)$^{-1}$
S_{22}'	0.112×10^{-6} (psi)$^{-1}$ (s)$^{-q}$
S_{66}^0	0.986×10^{-6} (psi)$^{-1}$
S_{66}'	0.476×10^{-6} (psi)$^{-1}$ (s)$^{-q}$
q	0.05
τ_c	$(6530)^2$ (psi)^2
r	1.7
c_3	4.2
c	4.0
ν_{23}	0.738
A	1.57×10^{-13}

In practice, the power law is not an exact representation of the actual behavior, and therefore it may be better to use more than one compliance to evaluate the constants. Mignery[6] employed data for S_{22} and S_{66} (in only the nonlinear range) from in-plane loading of $[90]_{8T}$ and $[\pm 40]_{2S}$ laminates (at the same constant load rate used for the single-lap joints) to derive A, r, τ_c and c_3; in the subsequent lap joint analysis it was assumed that $c_2 = c_3$ and $c_1 = 1 - c/2$, where c is given by Eq. (11b) and ν_e is the (constant) matrix Poisson's ratio. It should be noted that this process yielded from nonlinear data $c_3 \simeq 4.2$, whereas $c_3 \simeq 3.4$ from Eq. (19c).

Table I gives the results of the characterization. The material constants were used for all calculations here and in Reference [6]. That the resulting constitutive equations are valid for data other than that used to derive the material constants was shown by successfully predicting the Poisson's ratio of the $[\pm 40]_{2S}$ laminate in the linear and nonlinear ranges of behavior.[6]

APPLICATION OF THE MATERIAL MODEL IN A FINITE ELEMENT ANALYSIS

A commercially available finite element program (ABAQUS) was chosen which accommodates a user-supplied subroutine for the constitutive model of an element. Due to the eccentricity of load path in the single-lap joint, large displacement theory must be used to analyze the boundary value problem. For this type of analysis, ABAQUS uses the Updated Lagrangian Form, thereby calling upon the incremental form of the stiffness matrix. But we have characterized the total strains in terms of complementary work, which leads directly to the compliances of the lamina. Therefore, the incremental form of the compliance matrix needs to be developed first and then numerically inverted for use in the finite element solution.

For the linear range, the incremental compliance matrix is the same as the compliance matrix. For the nonlinear case, differentiation is required to arrive at

the incremental form. The result can be written as

$$\Delta\varepsilon_i = \hat{S}_{ij}\,\Delta\sigma_j \tag{20}$$

where the incremental compliances $\hat{S}_{ij}$ are

$$\hat{S}_{ij} = \frac{\partial^2 W_0}{\partial\sigma_i\,\partial\sigma_j} + \left[\frac{\partial W_1}{\partial\tau_s}\frac{\partial^2\tau_s}{\partial\sigma_i\,\partial\sigma_j} + \frac{\partial^2 W_1}{\partial\tau_s^2}\frac{\partial\tau_s}{\partial\sigma_i}\frac{\partial\tau_s}{\partial\sigma_j}\right]t^q \tag{21}$$

where W_0 and W_1 are in Eqs. (8) and (9), respectively. Completing the differentiation yields a symmetric incremental compliance matrix as given below:

$$\begin{Bmatrix}\Delta\varepsilon_{11}\\ \Delta\varepsilon_{22}\\ \Delta\varepsilon_{33}\\ \Delta\gamma_{23}\\ \Delta\gamma_{13}\\ \Delta\gamma_{12}\end{Bmatrix} = \begin{bmatrix}\hat{S}_{11} & \hat{S}_{12} & \hat{S}_{13} & 0 & 0 & 0\\ \hat{S}_{12} & \hat{S}_{22} & \hat{S}_{23} & \hat{S}_{24} & \hat{S}_{25} & \hat{S}_{26}\\ \hat{S}_{13} & \hat{S}_{23} & \hat{S}_{33} & \hat{S}_{34} & \hat{S}_{35} & \hat{S}_{36}\\ 0 & \hat{S}_{24} & \hat{S}_{34} & \hat{S}_{44} & \hat{S}_{45} & \hat{S}_{46}\\ 0 & \hat{S}_{25} & \hat{S}_{35} & \hat{S}_{45} & \hat{S}_{55} & \hat{S}_{56}\\ 0 & \hat{S}_{26} & \hat{S}_{36} & \hat{S}_{46} & \hat{S}_{56} & \hat{S}_{66}\end{bmatrix}\begin{Bmatrix}\Delta\sigma_{11}\\ \Delta\sigma_{22}\\ \Delta\sigma_{33}\\ \Delta\sigma_{23}\\ \Delta\sigma_{13}\\ \Delta\sigma_{12}\end{Bmatrix} \tag{22}$$

in which

$$\begin{aligned}
\hat{S}_{11} &= S_{11}^0\\
\hat{S}_{12} &= S_{12}^0\\
\hat{S}_{13} &= S_{12}^0\\
\hat{S}_{22} &= S_{22}^0 + 2Ar\tau_s^{r-1}t^q + W_S\left(2\sigma_{22} + 2\sigma_{33}\left(1-\frac{c}{2}\right)\right)^2\\
\hat{S}_{23} &= -\nu_{23}S_{22}^0 + 2Ar\tau_s^{r-1}t^q\left(1-\frac{c}{2}\right) + W_s\left(2\sigma_{22} + 2\sigma_{33}\left(1-\frac{c}{2}\right)\right)\\
&\quad\times\left(2\sigma_{33} + 2\sigma_{22}\left(1-\frac{c}{2}\right)\right)\\
\hat{S}_{24} &= W_S\left(2\sigma_{22} + 2\sigma_{33}\left(1-\frac{c}{2}\right)\right)(2c_2\sigma_{23})\\
\hat{S}_{25} &= W_S\left(2\sigma_{22} + 2\sigma_{33}\left(1-\frac{c}{2}\right)\right)(2c_2\sigma_{13})\\
\hat{S}_{26} &= W_S\left(2\sigma_{22} + 2\sigma_{33}\left(1-\frac{c}{2}\right)\right)(2c_2\sigma_{12})\\
\hat{S}_{33} &= S_{22}^0 + 2Ar\tau_s^{r-1}t^q + W_S\left(2\sigma_{33} + 2\sigma_{22}\left(1-\frac{c}{2}\right)\right)^2\\
\hat{S}_{34} &= W_S\left(2\sigma_{33} + 2\sigma_{22}\left(1-\frac{c}{2}\right)\right)(2c_2\sigma_3)\\
\hat{S}_{35} &= W_S\left(2\sigma_{33} + 2\sigma_{22}\left(1-\frac{c}{2}\right)\right)(2c_2\sigma_{13})
\end{aligned} \tag{23}$$

$$\hat{S}_{36} = W_S\left(2\sigma_{33} + 2\sigma_{22}\left(1 - \frac{c}{2}\right)\right)(2c_2\sigma_{12})$$

$$\hat{S}_{44} = 2(1 + \nu_{23})S^0_{22} + 2c_2 A r \tau_s^{r-1} t^q + W_S(2c_2\sigma_{23})^2$$

$$\hat{S}_{45} = W_S(2c_2\sigma_{13})(2c_2\sigma_{23})$$

$$\hat{S}_{55} = S^0_{66} + 2c_2 A r \tau_s^{r-1} t^q + W_S(2c_2\sigma_{13})^2$$

$$\hat{S}_{56} = W_S(2c_2\sigma_{13})(2c_2\sigma_{12})$$

$$\hat{S}_{66} = S^0_{66} + 2c_2 A r \tau_s^{r-1} t^q + W_S(2c_2\sigma_{12})^2$$

where

$$W_S \equiv \frac{\partial^2}{\partial \tau_s^2}(W_1 t^q) = Ar(r-1)\tau_s^{r-2} t^q \tag{24}$$

Numerical inversion then gives the incremental moduli. These must then be transformed by rotation to the finite element structural axis system.

Standard transformation matrices are used for this rotation giving

$$\{\Delta\tilde{\sigma}\} = [\tilde{c}]\{\Delta\tilde{\varepsilon}\} \tag{25}$$

where $\{\Delta\tilde{\sigma}\}$ and $\{\Delta\tilde{\varepsilon}\}$ are the incremental stresses and strains in the finite element coordinate system and $[\tilde{c}]$ is the transformed incremental stiffness matrix. Note that there are still six components of stress and strain in the above equation. Plane stress elements are used in the finite element analysis, which will be discussed further below. Imposing plane stress ($\Delta\tilde{\sigma}_{zz} = \Delta\tilde{\sigma}_{yz} = \Delta\tilde{\sigma}_{xz} = 0$) on Eq. (25) gives

$$\begin{Bmatrix} \Delta\tilde{\sigma}_{xx} \\ \Delta\tilde{\sigma}_{yy} \\ \Delta\tilde{\sigma}_{xy} \end{Bmatrix} = \begin{bmatrix} \tilde{c}^*_{11} & \tilde{c}^*_{12} & \tilde{c}^*_{13} \\ \tilde{c}^*_{12} & \tilde{c}^*_{22} & \tilde{c}^*_{23} \\ \tilde{c}^*_{13} & \tilde{c}^*_{23} & \tilde{c}^*_{33} \end{bmatrix} \begin{Bmatrix} \Delta\tilde{\varepsilon}_{xx} \\ \Delta\tilde{\varepsilon}_{yy} \\ \Delta\tilde{\gamma}_{xy} \end{Bmatrix} \tag{26}$$

in terms of plane stress moduli $\tilde{c}^*$. A complete reduction of Eq. (25) to Eq. (26) can be found in Ref. [6].

For a standard finite element modeling of one layer of elements per composite ply, the above formulation is used by giving the appropriate angle of each lamina and the corresponding material properties S_{11}, S_{12}, S^0_{22}, S^0_{66}, A, r, q, c, c_3 and ν_{23}. Their values are in Table I. The through-thickness Poisson's ratio ν_{23} was determined from standard micromechanical equations.[11]

If this ply-by-ply modeling is used with the angle-ply laminate for a standard tensile sample configuration, the resulting strain is that of a unidirectional lamina. This inconsistency is caused by the condition of plane stress used for the finite element system. In reality, for the angle-ply (neglecting free-edge effects) a further condition exists:

$$\Delta\tilde{\gamma}_{xz} = \Delta\tilde{\gamma}_{yz} = 0 \tag{27}$$

Equation (26) for plane stress does not satisfy Eq. (27) because the plies are considered individually. We must first model each pair of $\pm\theta$ plies. In order to avoid a full three-dimensional analysis, but still account correctly for angle-ply

orientation, we have lumped the ply pair into one element and then required the element strains $\Delta\bar{\gamma}_{xz}$ and $\Delta\bar{\gamma}_{yz}$ to be zero. For the matrix given in Eq. (25), this leads to angle-ply coefficients which satisfy

$$\begin{aligned} &\bar{C}_{15}=\bar{C}_{13}, \quad \bar{C}_{25}=\bar{C}_{23}, \quad \bar{C}_{35}=\bar{C}_{33}, \quad \bar{C}_{56}=\bar{C}_{36}, \quad \bar{C}_{14}=\bar{C}_{15}, \\ &\bar{C}_{24}=\bar{C}_{25}, \quad \bar{C}_{34}=\bar{C}_{35}, \quad \bar{C}_{44}=\bar{C}_{45}, \quad \bar{C}_{46}=\bar{C}_{56} \end{aligned} \tag{28}$$

thus simplifying the expressions derived for $\bar{c}_{ij}^{*}$ of Eq. (26); they can be found in detail in Ref. [6]. It should be emphasized that ply equations (22) and (23) were used to predict behavior of each angle-ply pair, and the result was used in a plane stress, finite element formulation. From the strain response of each ply pair, one may calculate the stresses within each ply using the ply theory, Eq. (22).

FINITE ELEMENT MODEL OF THE JOINT ASSEMBLY

Shown in Figure 3 is the type of mesh used for analysis of the adhesive joint. The particular mesh shown was used for the aluminum and 0° unidirectional composite adherend assemblies; for the angle-ply $[\pm 40°]_{2S}$ laminate each ± 40 ply-pair was represented by one element in the y direction, and by the same size elements in the x direction shown in Figure 3. In all analyses plane stress was assumed, in that for the forces/area acting on the ply-pairs, $\sigma_z = \tau_{xz} = \tau_{yz} = 0$, where z is normal to the page. (With aluminum adherend testing and strain prediction we found that plane stress conditions worked well in the straps and joint, although there is clearly a three-dimensional stress state in and close to the overlap region and the grips.) For the unidirectional laminate, the solution was found by iteration on the stresses σ_x, σ_y, τ_{xy}. However, iteration on the *six* lamina stresses in the principal material coordinate system was used for the angle-ply laminate.

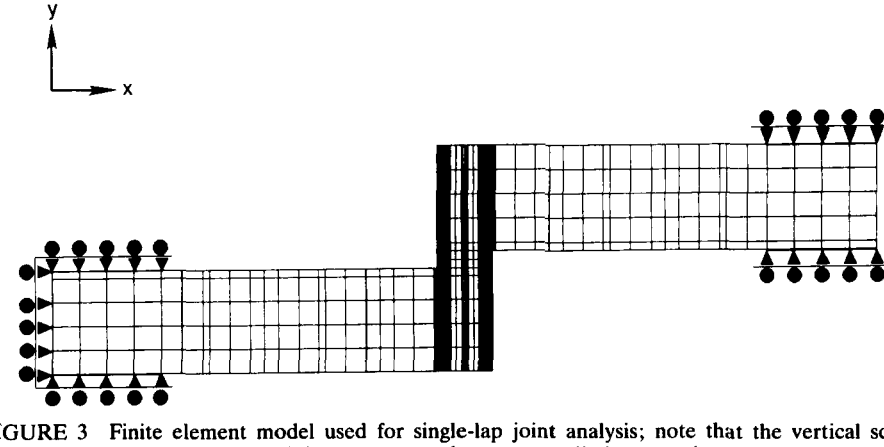

FIGURE 3 Finite element model used for single-lap joint analysis; note that the vertical scale is greatly expanded. The wide solid lines represent the many small elements shown in Figure 11.

As noted previously, all structural analyses were made with the finite element software package ABAQUS, augmented with the above material model. Pre- and post-processing routines were developed to evaluate finite element mesh designs and predict strains. Eight-noded 2D continuum isoparametric elements were used throughout. Shown in Figure 3 is the typical model used along with boundary conditions which match the experimental, non-rotating grip application. The total length of the mesh is 7.5 in. with a 0.5 in. overlap and thicknesses of 0.06 in. and 0.05 in. for the aluminum and composite adherends (respectively) and 0.006 in. for the adhesive. Two layers of elements were used through the adhesive thickness. Strain gage areas were modeled by one element (in the x-direction) in the straps, six elements at the edge of the overlap, and three elements in the center of the overlap. The strain predictions used were an average of the nodal strains of the elements in these areas. Most predictions were made using geometrically nonlinear elements. Although not discussed in detail here, predictions using geometrically linear finite elements are included in the results for comparison. These are designated later by the letters LFE in the figure legends.

Composite properties uses for all analyses are given in Table I. Linear elastic material properties were used for the adhesive in all cases; these were taken as handbook values, $E = 7.0 \times 10^5$ psi, $\nu = 0.40$. For the aluminum, $E = 10.2 \times 10^6$ psi and $\nu = 0.33$. Time increments for the finite element analysis were scaled inversely with the rates used for the experimental tests, 5 lb/s and 0.05 lb/s until failure. The FE theory is plotted using points, and the points indicate the actual steps used in the analysis.

The effects of geometric nonlinearity, which are primarily due to transverse displacement of the straps rather than large strains, are illustrated in Figure 4 for

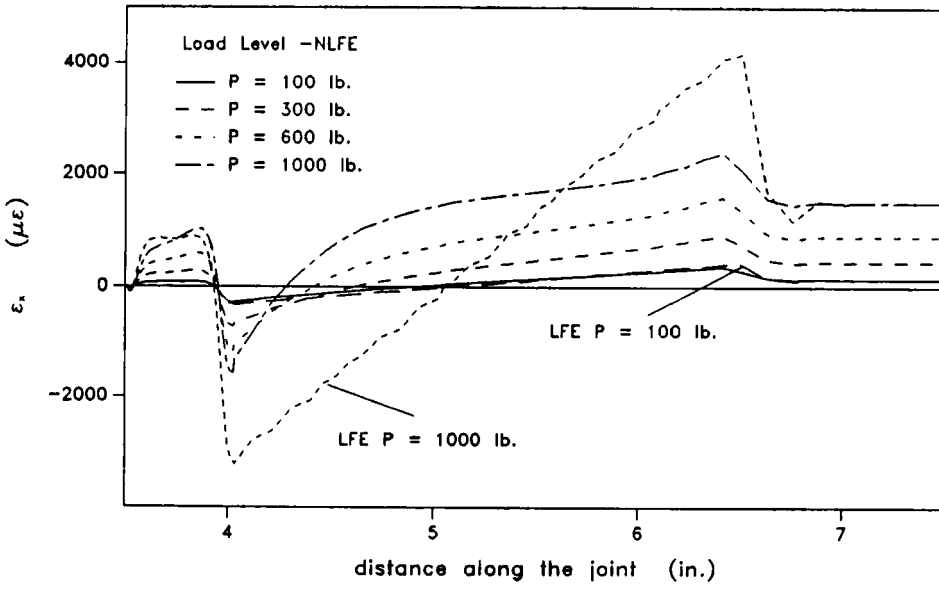

FIGURE 4 Predicted axial strains in top surface of aluminum adherend in a single-lap joint.

aluminum adherends. The strains at the far right end in the grip region are essentially those for a bar under uniform axial stress. In most of the strap the strain is due primarily to axial stretching plus simple bending. The difference between the strain in the strap and in the grip region is therefore due to bending. It is seen that linear theory (LFE) predicts a considerable amount of strain due to bending. However, at the highest loads the strain due to bending over a wide central portion of the strap is quite small compared with the total strain. Indeed, for high loads, in this region the strain response is *approximately the same as for a bar under uniform, uniaxial tension.*

In the Appendix, classical beam theory is used to obtain analytical solutions for the lap-joint specimen with and without large displacement effects. This theory has been found to agree with the strains in Figure 4 (except close to overlap and grip) and in Figure 5. Thus, one may consider the results in Fig. 4 to be representative for any linear material; the effect of different values of axial modulus disappears when load/modulus, instead of load is used as the parameter.

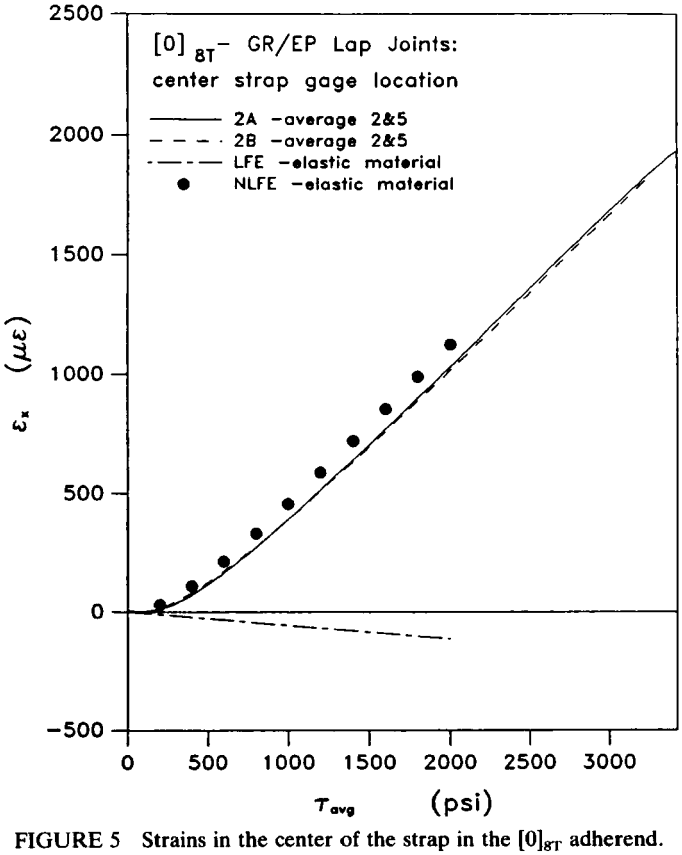

FIGURE 5 Strains in the center of the strap in the $[0]_{8T}$ adherend.

RESULTS AND DISCUSSION

Fracture behavior and three-dimensional (width) effects

Failure of the 0° adherend and aluminum specimens always occurred in the adhesive. For the 0° assembly, failure strength (the failure load divided by the bond area) was approximately 3500 psi; for aluminum it was 2500 psi, in agreement with the manufacturer's given strength. With regards to the viscoelasticity of the angle-ply adherend specimens, experimental results generally indicated that a redistribution of strain occurred in the single-lap joint with load rate. Failure was found to occur always in the overlap region, but in the adherend for the fast rate and in the adhesive for the slow rate. The failure strength of this assembly was approximately 2250 psi for the slow rate and 2750 for the fast rate. A detectable three-dimensional failure occurred with the slow rate, in that a thumb-nail type of curved striation pattern was present on the fracture surface of the adhesive layer.

No significant three-dimensional effects were seen with the strain gages 7–12 (Figure 1) at the edge of the overlap for the 0° and aluminum specimens. However, marked three-dimensional readings were observed in the angle-ply system. Gage readings from the outer width locations (gages 7, 9, 10, and 12) were typically 50 percent higher than those in the center of the width (gages 8 and 11). The degree of three-dimensionality was more pronounced in the fast rate tests. That the three-dimensional effects are so large is not surprising in view of the high Poisson's ratio of the angle-ply laminate; it is approximately 1.0 in the linear range and 1.3 at high strains.

Experimental strain readings and finite element predictions

Strains at three of the four gage locations will be discussed for the two composite adherend systems. (Good agreement with theory was found for the aluminum adherends.[6]) The gages at the center strap location, 2 and 5, provide a look at a region of more beam-like behavior than in the overlap region. The central and edge readings for the overlap will be investigated as well.

$[0]_{8T}$ Adherends

Unlike the angle-ply, the 0° laminate is free from significant material nonlinearity and rate effects in the straps. Shown in Figure 5 are the strain measurements in the center strap location from two samples with 0° adherends and predictions using linear and nonlinear elastic finite element methods (LFE and NLFE); the abscissa is the average applied shear stress (*i.e.*, axial load/overlap area). The measured axial strains are from 5 lb/s tests to failure, and are an average of the strain readings from gage 2 and gage 5. It can be seen that the experimental strain variations at this gage location are nonlinear with respect to the applied load. Considering the material linearity of the 0° adherend and how small the strains are, the nonlinearity is obviously due to large displacements. The two theoretical

predictions given in this figure were both made using a linear material model. It is seen that the plane stress, geometrically nonlinear finite element prediction is close to the experimental response.

Figure 6 shows results for the center of the overlap gage location in the 0° adherend single-lap joint. Once again, the axial strain is plotted against the average applied shear stress. The axial strain is an average of the readings from gage 3 and gage 4 for each of the two samples shown, 2A and 2B. Experimental data indicate nearly linear behavior to failure for this gage location. Of all gage locations monitored, this location was the only one to demonstrate near-linearity. This is reasonable since it is located in a region where the bending moment vanishes. Two finite element predictions are given in this figure. The first is from geometrically linear finite element theory using the initial ($t = 0$) lamina compliances (LFE). Geometrically linear and nonlinear predictions give the same result. As can be seen, this finite element result under-predicts the experimental results. As shown, recalculation with the time dependent linear viscoelastic compliances greatly improved the predictions (NLFE–LVE) because of the

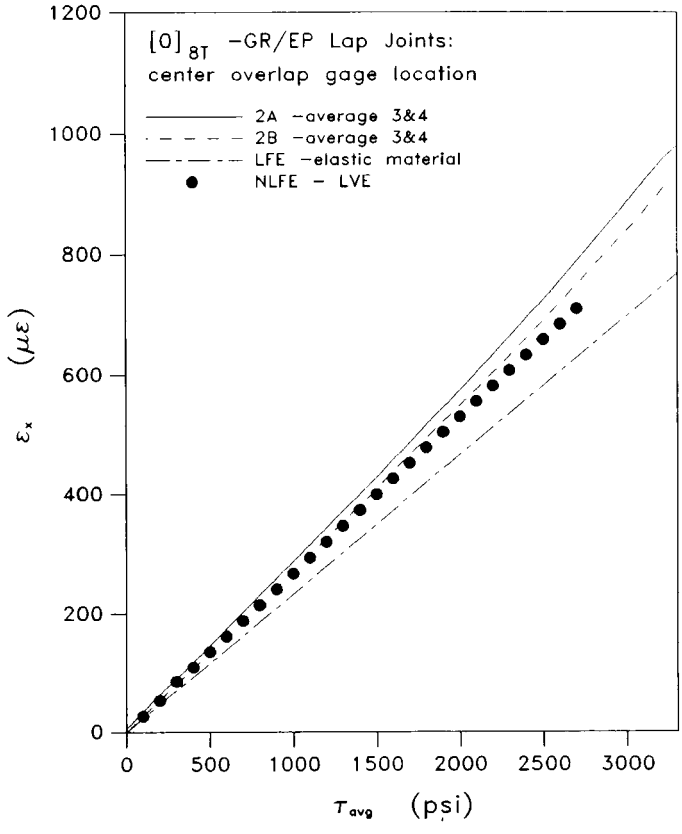

FIGURE 6 Strains at the center of the overlap in the $[0]_{8T}$ adherend.

contribution from the transient component of the shear compliance. This time-dependence was not observed with the aluminum adherends, and thus is not due to the adhesive. The gage location is in an area which is sensitive to the through-thickness shear modulus, wheras the center of the strap is essentially in a state of uniform tension, and thus is dependent only on the (constant) axial modulus of the adherend.

The final presentation for the 0° strain readings and predictions is that for the edge of the overlap. These are shown in Figure 7. The experimental values given are an average of all six strain readings at the overlap edge. As with the near grip location, the strain is nonlinear with the applied load. Calculations of the strain with geometrically linear finite elements (LFE) greatly over-predicts the strain magnitudes, while geometrically nonlinear elements using only the initial time-independent compliances (NLFE) predict the strain response fairly well; the remaining difference has been found to be due primarily to spew fillets, as discussed later for the angle-ply adherend.

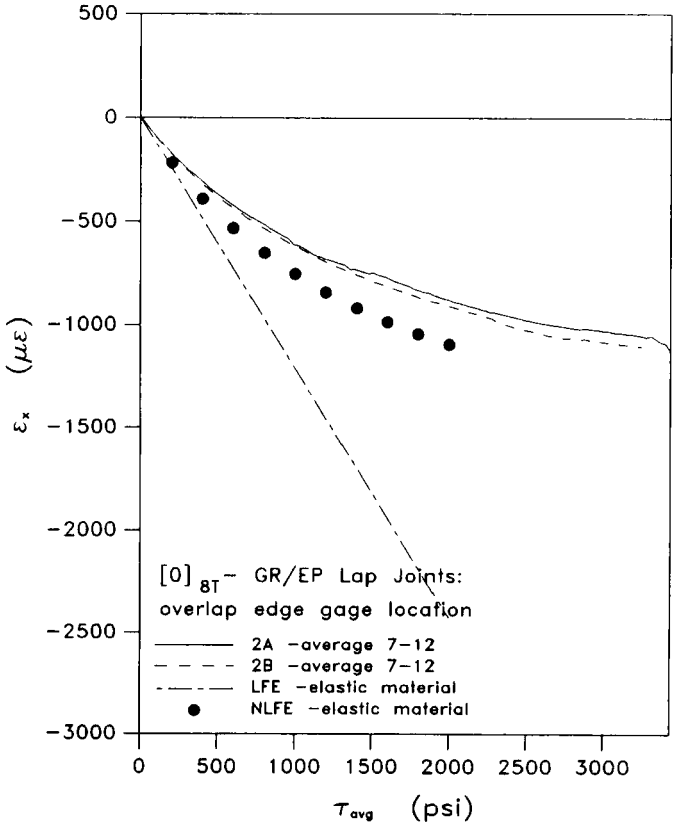

FIGURE 7 Strains at the edge of the overlap in the $[0]_{8T}$ adherend.

$[\pm 40]_{2S}$ Adherends

Experimental strain readings and their predictions for the angle-ply adherend assembly are given in Figures 8–10 for the same gage locations as presented in the 0° adherend discussion. Agreement between experiment and nonlinear theory is clearly not as good as for the 0° layup. Figure 8 shows the results for the center of the legs. Two samples were tested at each rate, with similar results, although for clarity of discussion data from only one sample are shown for each rate. The experimental data, which are the average of the readings from gages 2 and 5, are not shown out to failure due to the strain limit of the gages. Notice the strain range is almost ten times that for the 0° laminate. The effect of loading rates in the angle ply system is also clearly demonstrated.

This rate dependence has been found to be much greater than for uniaxial tensile samples of the *same* layup. It could be argued that the lap joint configuration produces more time dependence due to the complex state of stress; however, calculations indicate that the center of the strap is practically in a state

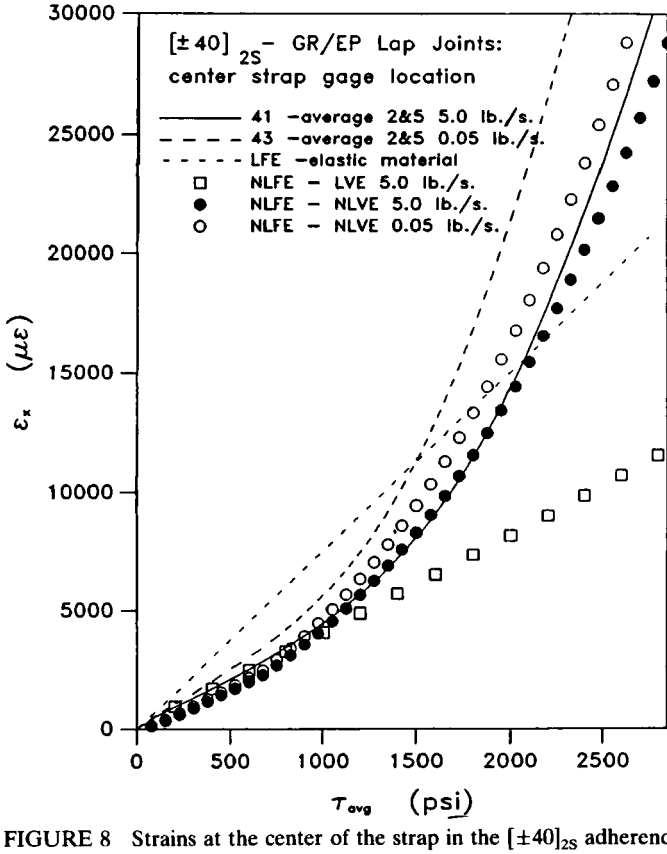

FIGURE 8 Strains at the center of the strap in the $[\pm 40]_{2S}$ adherend.

of pure extension. Strains should, therefore, show the same amount of rate dependence as seen in tensile samples. During development testing of the material model, the mesh for the outer leg was used for a tensile sample. Time dependence of the tensile strain in the angle-ply composite was predicted quite well using unidirectional ply data, yet in the lap-joint it was not. This indicates that errors due to mesh size and laminate analysis do not account for the discrepancy between theory and experiment in Figure 8. Also, material constants used in the finite element calculations were determined using the same loading rate as in the lap-joint experiments. Since the discrepancy between theory and experiment for the lap-joint occurs throughout in the loading sequence, it is unlikely that a propagation of any uncertainty in experimental measurements could cause this difference. Rather, moisture absorption and/or aging are believed to account for the greater time dependence as these tests were conducted many months after the characterization was done and the composite used is sensitive to moisture. Also, the time required for sample preparation (and consequent exposure to atmospheric moisture) was much greater for the joints

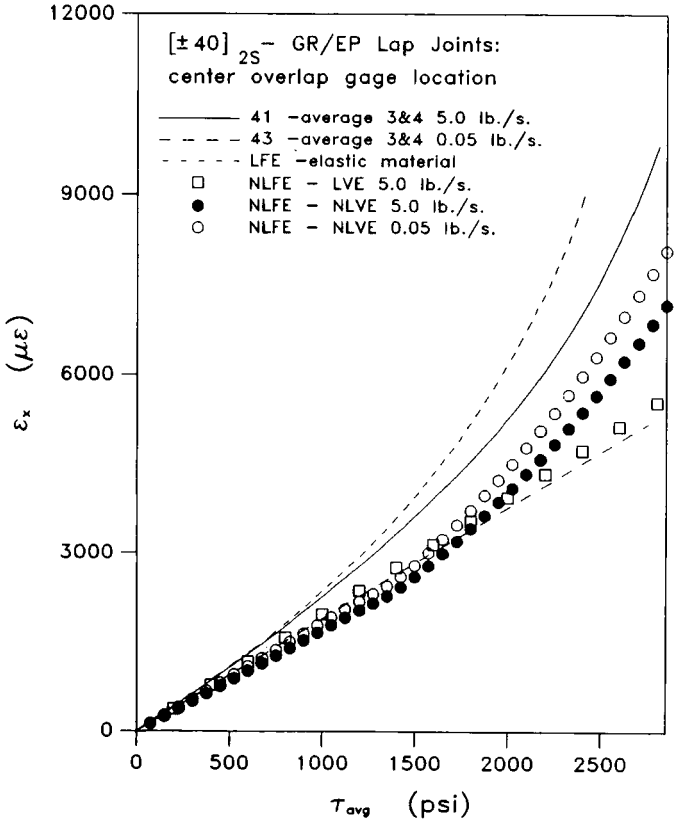

FIGURE 9 Strains at the center of the overlap in the $[\pm 40]_{2S}$ adherend.

than for the laminates used in material characterization, although the full size plates were stored with desiccant prior to fabricating the joints. In order for the data from the lap-joints to match the theoretical time-dependence more closely, the composite used for the material characterization should have travelled along with the adhesive joints throughout the program.

Results from the geometrically nonlinear, but materially linear, viscoelastic analysis (NLFE–LVE) show the limited range of data which are predictable without the addition of the nonlinear material model.

Results at the center of the overlap in the angle-ply adherend case are shown in Figure 9. It can be seen that the experimental strain is nonlinear with respect to the applied load, indicating again the strong material nonlinearity. The moment is zero at this location and thus it is a region of geometric linearity. That the experimental strains are noticeably higher than predicted from the plane stress theory is believed due to three-dimensional effects stemming from the high Poisson's ratio of the angle-ply layup; as noted previously, it is approximately 1.0 at the lowest strains and 1.3 at the highest strains. Namely, plane stress theory

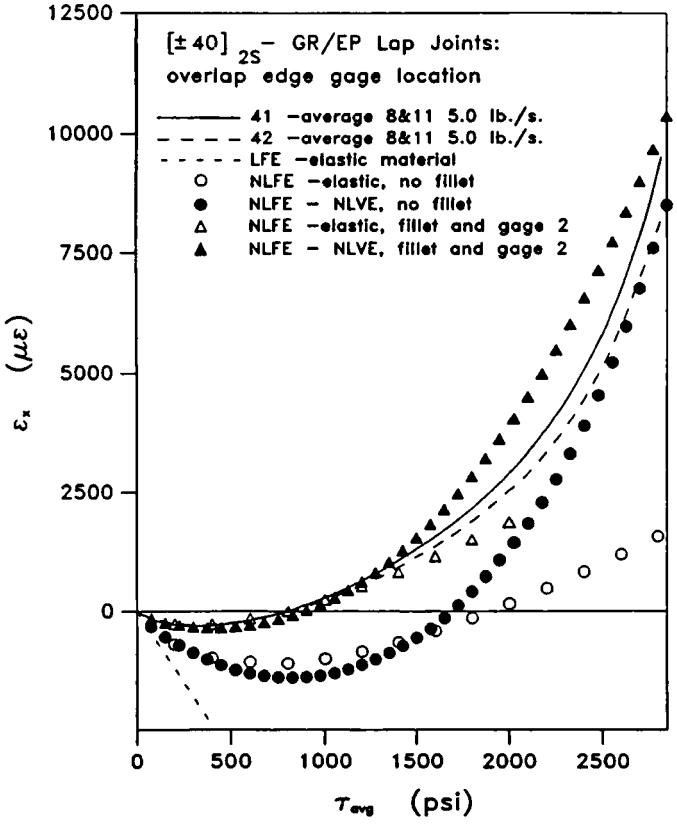

FIGURE 10 Strains at the edge of the overlap in the $[\pm 40]_{2S}$ adherend.

predicts transverse contraction (in the z direction) for the strap which is well over twice that in the center of the overlap. In the actual joint, the high strap contraction causes more transverse contraction and axial tensile strain in the overlap region than predicted by plane stress theory.

The final strains to be investigated are at the edge of the overlap, Figure 10. The gage readings are now an average of gages 8 and 11 at the center of the width; due to the strong three dimensionality (arising from the high Poisson's ratio) of this angle-ply laminate and the geometry of the overlap, the strains near the edges (gages 7, 9, 10, and 12) were not used in the comparison with predictions based on plane stress. The readings in Figure 10 are quite different from those in Figure 7 for the 0° adherend system, in that there is now an increase in strain after the initial decrease. Predictions with the various material and geometric models are indicated in the legend. It can be seen that the only good prediction for the "no fillet" case is at high strains with the full material and geometrically nonlinear model.

That the small strain range cannot be predicted makes one suspect that the source of error is not the material modeling, but the geometric modeling. Indeed, an examination of the samples showed that a small adhesive spew fillet was present on all samples. This is unavoidable in the fabrication process. Samples showed the excess adhesive to extend half way up the side of the adherend thickness and an equal distance along the leg, accounting for a size of approximately 0.025 in. in both directions. This area was modeled with the finite element mesh shown in Figure 11. Given is an enlargement of the overlap area; note that the thickness scale in Figure 11 has been greatly expanded. The

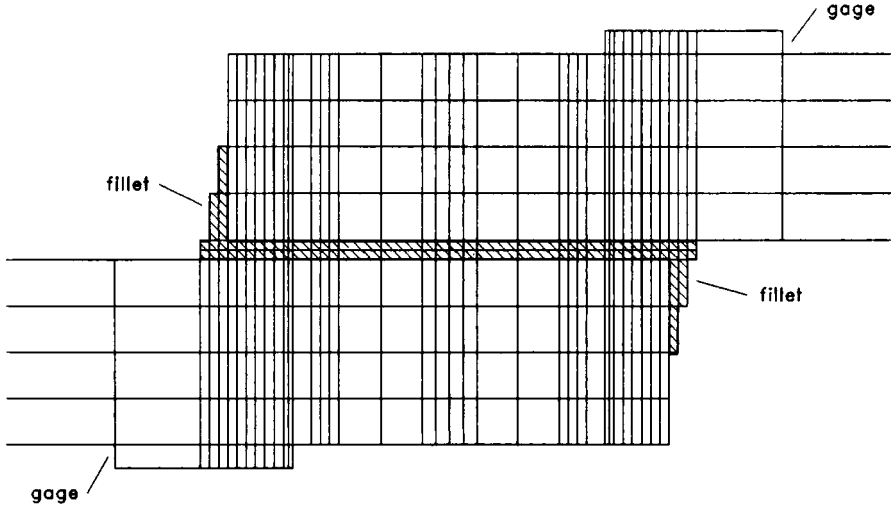

FIGURE 11 An enlargement of the overlap region of the finite element model indicating addition of the adhesive fillet at the edge of the overlap for the $[\pm 40]_{2S}$ adherend. The cross-hatched region indicates the adhesive layer and the fillet.

cross-hatched region in the figure indicates the fillet and adhesive layer. Also modeled are the strain gages at the edge of the overlap; predictions with the stiffening effect of the gages ($E \simeq 10^6$ psi, $\nu \simeq 0.4$) were nearly the same as without it, although with the gages the predictions were closer to the experimental strains. Predictions using this model with fillets are given in Figure 10. The material and geometrically nonlinear analyses with and without the fillets are seen to bound the experimental data. The behavior is believed to be indicative of the failure of this joint; cracking began at the fillet and, therefore, the early predictions need the fillet stiffness for correspondence with experimental results. After cracking begins, the model without a fillet is closer to the experimental sample. The inclusion of the fillet did not alter any predictions at other locations.

CONCLUSIONS

The mechanical behavior of aluminum and composite adherends in single lap joint assemblies has been studied experimentally and theoretically. Most of the results shown are for adherends made of 0° unidirectional and ±40° angle-ply layups of a rubber toughened graphite/epoxy. Agreement between theory and experiment for surface strains in the overlap region and straps is quite good for most cases in spite of the large geometric nonlinearity; however, material variability possibly due to aging and/or moisture caused discrepancies, especially at the lowest rate with the angle-ply adherends. The angle-ply layup was selected to enable study of significant nonlinearity and time (or rate) effects, and thus provide a severe test of the constitutive theory and structural analysis method. The Poisson's ratio for this layer exceeds unity, which produced noticeable three-dimensional effects in the overlap region. The strains at the edge of the overlap were shown to be sensitive to adhesive spew fillets; these fillets were needed in the finite element model in order to bring theory and experiment into fair agreement. It was also found that an analytical solution (based on classical nonlinear beam theory) for strains in the aluminum and 0° laminate straps agree well with the finite element analysis.

Overall, this study has shown how complex the mechanical response of adhesively bonded composite joints is. Yet many of the features of the strain response can be predicted. No attempt was made to predict the effect of loading rate and layup on joint strength, such as the observation that the joint failed in the angle-ply adherend at the highest rate and in the adhesive at the lowest rate. However, it is believed that the three-dimensional constitutive theory and type of structural analysis used here could be employed in a more detailed study of the mechanical state and strength of bonded composite joints. Failure due to crack growth could be investigated by accounting for defects such as an adherend delamination or a crack in the adhesive layer.

Acknowledgement

The authors are grateful to the Naval Air Development Center and Office of Naval Research for sponsoring this investigation.

References

1. R. D. Adams and W. C. Wake, *Structural Adhesive Joints in Engineering* (Elsevier Applied Science Publishers LTD, London, 1984).
2. R. A. Schapery, A theory of mechanical behavior of elastic media with growing damage and other changes in structure, *J. Mech. Phys. Solids*, **38**, 215 (1990).
3. R. A. Schapery, A method for mechanical state characterization of inelastic composite laminates with damage, in *Proc. Seventh Int. Conf. on Fracture* (Pergamon, New York, 1989, p. 2177.
4. Y. C. Lou and R. A. Schapery, Viscoelastic characterization of a nonlinear fiber-reinforced plastic, *J. Composite Materials* **5**, 208 (1971).
5. C. T. Sun and J. L. Chen, A simple flow rule for characterizing nonlinear behavior of fiber composites, in *Sixth International Conference on Composite Materials ICCM & ECCM Second European Conference on Composite Materials* (Elsevier Applied Science Publishers LTD, London, 1987, p. 1.250.
6. L. A. Mignery, Viscoelastic adherend effects in adhesively bonded composite-to-composite joints, Ph.D. Dissertation, Texas A & M University, (Dec. 1988).
7. R. A. Schapery, Mechanical characterization and analysis of inelastic composite laminates with growing damage, *Mechanics of Composite Materials and Structures, ASME AMD* **100**, 1 (1989).
8. Hibbitt, Karlsson, and Sorenson, *ABAQUS*, Providence, RI, Version 4.5 (1985).
9. R. A. Schapery, A method of viscoelastic stress analysis using elastic solutions, *J. Franklin Institute* **279**, 268 (1965).
10. M. J. Lamborn and R. A. Schapery, An investigation of deformation path-independence of mechanical work in fiber-reinforced plastics, *Proc. 4th Japan-U.S. Conference on Composite Materials* (Technomic Publishing Co., Lancaster, PA, 1988), p. 991.
11. S. W. Tsai and H. T. Hahn, *Introduction to Composite Materials* (Technomic Publishing Co., Lancaster PA, 1980).

Appendix. Beam Theory

Consider the single-lap joint structural idealization in Figure 12. Classical linear and nonlinear beam theory will be used to predict the moment and strain distributions along the length.

The pinned connection at the left end is located at the center of the adhesive layer in the actual joint. The additional rigidity due to the two overlapping adherends is neglected. As shown in the free body diagram, the horizontal shear load P at the pin is statically equivalent to a central axial load and bending moment,

$$M_1 = Ph_1 \tag{1A}$$

where

$$h_1 = (h + h_a)/2$$

h = adherend thickness

h_a = adhesive thickness

It turns out that a tensile load acts normal to the adhesive layer, which is shown as the vertical pin reaction V. Overall moment equilibrium gives the grip moment as

$$M_0 = M_1 - VL \tag{2A}$$

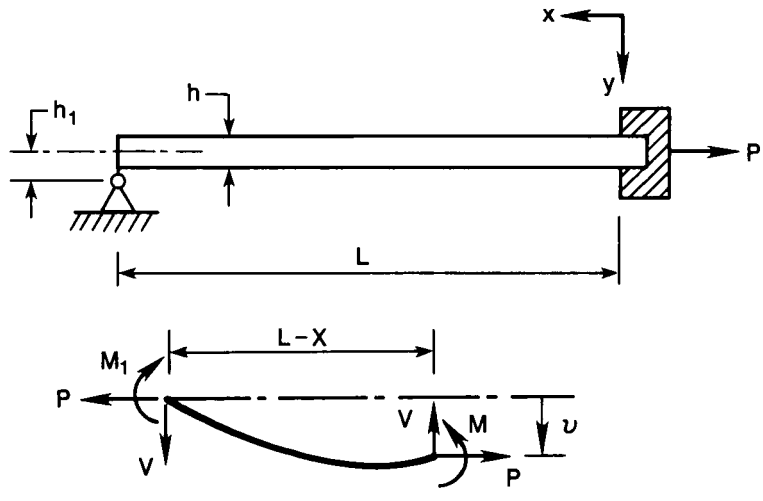

FIGURE 12 Structural idealization of a strap in the single-lap joint assembly. Top: Strap and idealized end conditions. Bottom: Free body diagram showing deformed strap centerline.

Also, for any moment distribution M, the axial strain in the top surface layer is

$$\varepsilon_x = (P/Bh - Mh/2I)/E \tag{3A}$$

where B is the beam width and $I = Bh^3/12$.

Linear beam theory yields

$$M = -M_1(1 - 3x/L)/2 \tag{4A}$$

and

$$M_0 = -M_1/2, \qquad V = 1.5M_1/L \tag{5A}$$

which may be substituted into Eq. (3A) to find ε_x. The linearly varying strain in Figure 3 is found to be in good agreement with this result.

Accounting now for the effect of vertical displacement on the internal bending moment, we obtain from Fig. 12,

$$M = M_1 - P\upsilon + V(x - L) \tag{6A}$$

where υ is the centerline displacement in the y-direction. Using the standard equation $EId^2\upsilon/dx^2 = -M$ we find

$$\frac{d^2\upsilon}{dx^2} - k^2\upsilon = -\frac{M_1}{EI} - \frac{V(x - L)}{EI} \tag{7A}$$

where

$$k^2 \equiv P/EI \tag{8A}$$

Solution of Eq. (7A), together with the boundary conditions at $x = 0$ and $x = L$,

yields $v(x)$. In turn, use of Eqs. (2a) and (6A) gives finally

$$M = \frac{V}{k}\sinh kx + \left(-\frac{V}{k}\tanh kL + \frac{M_1}{\cosh kL}\right)\cosh kx \tag{9A}$$

$$M_0 = M_1(1-\xi)/(\cosh kL - \xi) \tag{10A}$$

$$V = \frac{M_1}{L}(\cosh kL - 1)/(\cosh kL - \xi) \tag{11A}$$

where

$$\xi \equiv \sinh kL/kL \tag{12A}$$

One may verify that Eqs. (9A)–(11A) reduce to the linear results in Eqs. (4A) and (5A) when $kL \ll 1$, and that Eq. (3A) is in good agreement with the finite element predictions in Fig. 3 (except near the ends, $x = 0$ and $x = L$) and in Figure 5.